Applied Catalysis B: Environmental 327 (2023) 122439

Contents lists available at ScienceDirect

Applied Catalysis B: Environmental

journal homepage: www.elsevier.com/locate/apcatb

Unraveling the time evolution and *post mortem* changes of nanometric MnOOH during *in situ* oxidation of ciprofloxacin by activated peroxymonosulfate

Yeison Núñez-de la Rosa [a], Luis Guillermo Cuadrado Durango [a], Moacir Rossi Forim [a], Otaciro Rangel Nascimento [b], Peter Hammer [c], José M. Aquino [a,*]

[a] Federal University of São Carlos (UFSCar), Departament of Chemistry, 13565-905 São Carlos, SP, Brazil
[b] University of São Paulo (USP), São Carlos Institute of Physics, Department of Physics and Interdisciplinary Science, 13560-970 São Carlos, SP, Brazil
[c] São Paulo State University (UNESP), Institute of Chemistry, Department of Physical Chemistry, 14800-900 Araraquara, SP, Brazil

ARTICLE INFO

Keywords:
Advanced oxidation process
Heterogeneous catalysis
Emerging contaminants
Hydroxyl radicals
PMS induced Mn(IV) reduction

ABSTRACT

Nanometric MnOOH compound was synthesized by a green approach, characterized, and used to remove ciprofloxacin (CIP) antibiotic by *in situ* chemical oxidation using peroxymonosulfate (PMS). The effects of varying concentrations of MnOOH, PMS and pH, on morphological, structural, chemical, and electrochemical changes were studied during and after the experiments. The CIP molecule was completely oxidized and partially mineralized (>60%) after 6 h under acidic conditions. The mechanism of CIP degradation was induced by PMS activated oxidants ($HO^{\bullet}$ and $^1O_2$) and, to a lesser extent, directly on the surface of MnOOH. The latter process was evidenced by transmission electron microscopy showing the formation of an amorphous shell (MnO_2) over MnOOH crystallites, as verified using X-ray photoelectron spectroscopy and the subsequent increase of the charge transfer resistance that hindered a further electron transfer to the PMS oxidant. Such behavior is recoverable when using a freshly prepared PMS solution.

1. Introduction

The constant need for freshwater supply is increasingly being affected by pollution and the effects of climate change, resulting in an unprecedented change in the water cycle. [1]. The consequences are water scarcity and poor quality for human consumption [2]. In turn, the quality of water for human consumption is directly associated with basic sanitation conditions, as well as the type of treatment methods used for the water supply and after its disposal [3].

Water contamination by organic pollutants, such as antibiotics, plasticizers, dyes, pesticides, *etc.*, has been the subject of numerous studies due to their persistence in the environment and potential impact on the environment and human health [4–7]. Le Coadou *et al.* [5] and Chow *et al.* [6] detected different amounts of synthetic organic compounds at trace levels, such as hormones, pharmaceuticals, polyfluoroalkyl substances, in bottled water in France and U.S.A. Other studies reported the presence of organic pollutants in several water sources all around the world [7–10]. The ingestion of these compounds can lead to serious health problems as endocrine disruption, reproductive problems, cancer, cardiovascular disease, obesity, and diabetes [11]. Therefore, the development of new technologies for the treatment of emerging pollutants is of high priority.

Among the available methods to treat distinct water sources contaminated with organic pollutants, the catalytic advanced oxidation processes [12] are an interesting option as they can produce highly oxidizing species, such as hydroxyl ($HO^{\bullet}$) and sulfate ($SO_4^{\bullet-}$) radicals as well as non-radical species like singlet oxygen ($^1O_2$). Although the latter oxidant shows a weaker action than radical species, it is highly selective

Abbreviations: CIP, ciprofloxacin antibiotic; CV, cyclic voltammetry; DMPO, 5,5-dimethyl-1-pyrroline *N*-oxide; ESR, electron spin resonance; EI, Electrochemical impedance; HRTEM, high-resolution transmission electron microscopy; $HO^{\bullet}$, hydroxyl radical; HPLC, high-performance liquid chromatography; MnOOH, manganese oxyhydroxide (as-prepared); 3-MnOOH, manganese oxyhydroxide after 3 h of treatment; 6-MnOOH, manganese oxyhydroxide after 6 h of treatment; $^1O_2$, singlet oxygen; PDS, peroxydisulfate; PMS, peroxymonosulfate; $SO_4^{\bullet-}$, sulfate radical; TEMP, 2,2,6,6-tetramethyl-4-piperidine; TOC, total organic carbon; UHPLC-QToF MS, ultra-high performance liquid chromatography coupled to a time-of-flight mass spectrometry; XRD, X-ray diffraction; XPS, X-ray photoelectron spectroscopy.

* Corresponding author.
E-mail address: jmaquino@ufscar.br (J.M. Aquino).

https://doi.org/10.1016/j.apcatb.2023.122439
Received 22 July 2022; Received in revised form 18 October 2022; Accepted 5 February 2023
Available online 8 February 2023

and can react through electrophilic addition reactions and electron abstraction [13]. All these oxidant species can be produced through homogeneous catalysis using metal ions (Co, Cu, and Fe) [14], solid metal oxides, mainly derived from Fe and Mn [15,16], and carbon-based compounds [17], using peroxydisulfate (PDS) or peroxymonosulfate (PMS) as main oxidizers. Once produced, $HO^{\bullet}$ and $SO_4^{\bullet-}$ radicals can react with organic compounds through *i*) hydrogen abstraction, *ii*) electron transfer, and *iii*) addition-elimination [18].

Considering the *in situ* activation of oxidants by metallic oxides, Mn compounds stand out due to their abundant availability in the Earth's crust, low toxicity, and variable oxidation states that enables electron transfer [19,20]. Kamagate *et al.* [15] reported the important role of MnO_2 to oxidize norfloxacin antibiotic as well as oxide-bound Mn(II) species to activate persulfate. The use of manganite ($Mn^{III}OOH$) showed similar performances towards organic oxidation and mineralization [15]. The issue of Mn(II) leaching was investigated by Liu *et al.* [21] through the use of a carbon layer over Mn_3O_4. The carbon-coated particles exhibited low values of charge transfer resistance for higher carbon amounts due to the improvement of electrical conductivity and oxidant activation. All these strategies are important to design better catalysts and avoid contamination with metallic ions. However, little attention is paid to the time evolution of the Mn oxide catalyst during and after activation (*post mortem*) using distinct oxidants, although it is crucial for the development of efficient catalysts.

Thus, the aim of the present work was to synthesize, characterize, and apply MnOOH oxyhydroxide nanoparticles to activate the PMS oxidant in the degradation of the ciprofloxacin (CIP) antibiotic. More specifically, the influence of MnOOH and PMS concentration as well as solution pH on the PMS activation have been studied. For this purpose, the main oxidants produced during the CIP degradation have been studied using electron spin resonance (ESR) and the produced organic intermediates were identified using liquid chromatography coupled to high-resolution mass spectrometry (UHPLC-QToF MS). In addition, to understand the deactivation process of MnOOH, the time evolution of the MnOOH morphology, crystalline structure, superficial oxidation state, and electrochemical parameters were investigated using high-resolution transmission electron microscopy (HRTEM), X-ray photoelectron spectroscopy (XPS), and electrochemical measurements. The results showed that although recoverable, the formation of an amorphous MnO_2 shell covering MnOOH crystallites is deleterious for further PMS activation due to an increase of the charge transfer resistance.

2. Materials and methods

2.1. Chemical reagents

All chemicals, including CIP (ciprofloxacin hydrochloride monohydrate, EMS), $KMnO_4$ (analytical reagent - a.r., Sigma Aldrich), $C_{12}H_{22}O_{11}$ (a.r., Synth), $MnSO_4$ (a.r., Sigma Aldrich), HNO_3 (a.r., Qhemis), NaOH (a.r., Impex), H_2SO_4 (a.r., JTBaker), PMS (available as Oxone®, $KHSO_5{\cdot}0.5KHSO_4{\cdot}0.5K_2SO_4$. a.r., Sigma Aldrich), DMPO (5,5-dimethyl-1-pyrroline *N*-oxide - a.r., CaymanChem), TEMP (2,2,6,6-tetramethyl-4-piperidine - a.r., Sigma Aldrich), $Na_2S_2O_3$ (a.r., Synth), CH_3OH (HPLC grade, JTBaker), and HCOOH (a.r., JTBaker) were used as received without prior treatment. All solutions were prepared using deionized water (Millipore Milli-Q Academic system, $\rho \geq 18.2$ MΩ cm).

2.2. Synthesis of MnOOH

MnOOH was prepared according to the procedure reported in the work of Crisostomo *et al.* [22] with some modifications. Briefly, 50 mL of a 0.19 mol L^{-1} $KMnO_4$ solution was slowly added under constant stirring to a previously prepared solution containing 0.5 g of sucrose in 7.5 mL of water in the presence of 0.75 mL of concentrated HNO_3 (65% *m/V*). Then, 10 mL of a 0.65 mol L^{-1} $MnSO_4$ solution was slowly dripped to the mixture. The resultant solution was refluxed at ~100 °C for 1 h. After hot filtration, the brown solid product was washed with deionized water and vacuum dried using a desiccator.

2.3. MnOOH characterization

X-ray diffraction (XRD) experiments were performed using a D8 Advanced ECO (Bruker) instrument in the reflection mode (Cu-Kα_1 radiation of 1.54 Å, 40 kV, and 25 mA) at a scanning rate of 1° min^{-1} from 10° to 80° (2θ). The surface morphology was analyzed using a TECNAI G^2 F20 (FEI) high-resolution transmission electron microscopy (HRTEM).

The surface elemental analysis of MnOOH was carried out by XPS using a commercial spectrometer (UNI-SPECS UHV) with a base pressure lower than 10^{-7} Pa. The Mg Kα line was used ($h\nu = 1254.6$ eV) as the ionization source and the pass energy of the analyzer was set to 15 eV. The inelastic background of the C 1s, O 1s, and Mn $2p_{3/2}$ high-resolution spectra was subtracted using the Shirley method. The composition was determined by the relative proportions of the peak areas corrected by the Scofield's atomic sensitivity factors with an accuracy of ±5%. The deconvolution of the experimental spectra was performed using a Voigtian type function, with Gaussian (70%) and Lorentzian (30%) combinations. The width at half height varied between 1.0 and 2.0 eV and the position of the peaks was determined with an accuracy of ±0.1 eV with respect to the hydrocarbon peak located at 295.0 eV.

Electrochemical impedance (EI) measurements (±10 mV of perturbation from 5 kHz to 1 mHz) and cyclic voltammetry (CV) measurements (20 mV s^{-1}) were performed in an acidified (H_2SO_4, pH 3) 0.1 mol L^{-1} Na_2SO_4 solution at ambient conditions and using a conventional three-electrode cell with a Pt foil and an Ag/AgCl/KCl (3 mol L^{-1}) as a counter and reference electrode, respectively. The working electrode was composed of a carbon paper substrate as current collector on which a slurry containing a mixture of MnOOH (75% *m/m*), prepared at different treatment times (as-prepared, 3 h, and 6 h), XC-72 carbon (20% *m/m* from Cabot) and polyvinylidene fluoride (5% *m/m* from Sigma Aldrich) was deposited by drop coating. The slurry was previously mashed in an agate mortar and dispersed in 500 μL of N-methyl pyrrolidone. Before electrochemical assays, the as-prepared electrodes were dried at 60 ºC for 12 h. All measurements were carried out in the dark.

To further confirm the oxidation state of manganese in MnOOH (before and during degradation experiments at specific time intervals), a potentiometric titration method originally described by Vetter and Jaeger [23] and adapted by Cheng *et al.* [24] was used. Briefly, 50 mg of MnOOH was dissolved in 25 mL of a 0.25 mol L^{-1} $FeSO_4$ solution acidified with H_2SO_4 (Eq. 1). Then, the solution was diluted to 100 mL with deionized water. The resulting mixture was titrated using a previously standardized 0.5 mol L^{-1} $KMnO_4$ solution (Eq. 2) to obtain the first endpoint (V_1). Subsequently, $Na_4P_2O_7{\cdot}10\ H_2O$ (solid) was added to the previous solution until a pH value between 6 and 7 was reached. Finally, titration was resumed (Eq. 3) until the second endpoint (V_2) was reached. The *x* value of the equations was calculated according to (Eq. 4).

$$MnOx{\cdot}mH_2O + (2x\text{-}2)Fe^{2+} + 2xH^+ \rightarrow Mn^{2+} + (2x\text{-}2)Fe^{3+} + (x{+}m)H_2O \quad (1)$$

$$5Fe^{2+} + MnO_4^- + 8H^+ \rightarrow 5Fe^{3+} + Mn^{2+} + 4H_2O \quad (2)$$

$$4Mn^{2+} + MnO_4^- + 8H^+ + 15H_2P_2O_7^{2-} \rightarrow 5Mn(H_2P_2O_7)_3^{3-} + 4H_2O \quad (3)$$

$$x = 1 + \left\{\frac{5 \times (V_0 - V_1)}{2 \times [(4 \times V_2) - V_1]}\right\} \quad (4)$$

where V_0 is the endpoint volume of the same $KMnO_4$ solution in the blank titration, *i.e.*, without MnOOH. The endpoint of each titration was determined using a potentiometer with a Pt electrode and an Ag/AgCl/KCl (3 mol L^{-1}) as reference electrode.

All previous measurements were carried out for the as-prepared MnOOH and after 3 h (3-MnOOH) and 6 h (6-MnOOH) of treatment.

For this purpose, before analysis, the catalyst samples were collected at specific times (3 and 6 h), filtered, washed three times with deionized water, and dried under vacuum in a desiccator for 12 h.

2.4. Oxidation and mineralization of CIP

The *in situ* chemical activation of PMS using MnOOH for the oxidation and mineralization of CIP (50 mg L^{-1} – see chemical structure in Fig. S1) was carried out in a glass vessel (1.5 L) equipped with a magnetic stirrer. The PMS solution was continuously added to the reaction vessel during experiments using a peristaltic pump at 0.12 mL min^{-1}. The effect of different parameters such as the solution pH (3.0, 7.0, and 10.0), MnOOH dosage (0.5, 1.0, and 2.0 g L^{-1}), and PMS concentration (1.0, 2.0, and 4.0 g L^{-1}) were evaluated. The solution pH was continuously monitored and adjusted by adding concentrated H_2SO_4 or NaOH solutions (5 mol L^{-1}). Other operational variables, such as the solution volume, treatment time, solution temperature, and stirring were kept constant at 1.0 L, 360 min, 25 °C, and 600 rpm, respectively. Samples were collected from the reaction mixture at predetermined time intervals, filtered through a 0.22 μm cellulose acetate cartridge, and quenched with excess $Na_2S_2O_3$ (1.0 mol L^{-1}), except when residual oxidant was quantified.

After optimization of the experimental conditions, a recycling test (5 consecutive degradation experiments) was carried out. For this purpose, after each run, the MnOOH compound was recovered by vacuum filtration, washed thoroughly with deionized water, and dried under vacuum before further use.

2.5. Analyses of degradation experiments

The evolution of the CIP concentration was monitored by high-performance liquid chromatography (HPLC, Shimadzu 20A) at 270 nm and using a core-shell C-18 reversed-phase column as the stationary phase (150 mm × 4.6 mm i.d., 5 μm particle size, 100 Å pore size, from Phenomenex®). A mixture of aqueous 0.1% (*V/V*) formic acid (eluent A) and methanol (eluent B) was used as the mobile phase in a gradient elution mode in the following sequence: from 10% to 90% of B in 10 min and then, back to 10% after 3 min. The last condition was kept for 2 min before subsequent analyses. The flow rate, injection volume, and temperature of the column were kept fixed at 1.0 mL min^{-1}, 25 μL, and 24 °C, respectively.

The intermediates formed during the CIP degradation process were determined by ultra-high performance liquid chromatography coupled to a time-of-flight mass spectrometry (UHPLC-QToF MS), according to a methodology described in Text S1, in the supplementary material section.

The short-chain carboxylic acids were also determined by HPLC. For such, a Rezex™ ROA-H column (300 mm × 7.8 mm i.d., 8 μm particle size, from Phenomenex®) as the stationary phase and a 2.5 mmol L^{-1} H_2SO_4 solution as the mobile phase were used at 0.5 mL min^{-1}. The carboxylic acids were identified by comparing their retention times with those of previously analyzed standards. The injection volume, detection wavelength, and the temperature of the column were 25 μL, 210 nm, and 23 °C, respectively.

Inorganic ions were also analyzed by HPLC with a conductivity detector (Shimadzu CDD-10A SP). For anion determination, a Shodex SI-52 4E column at 45 °C and 3.6 mmol L^{-1} Na_2CO_3 solution at 0.8 mL min^{-1} was used as the stationary and mobile phases, respectively. For this analysis, a chemically suppressor system (Thermo Scientific™ ACRS 500) pumping a regenerating solution of 3.6 mmol L^{-1} H_2SO_4 at 0.8 mL min^{-1} was used. Concerning cation determination, a Shodex YS-50 column at 40 °C and a mixture of 4.0 mmol L^{-1} oxalic acid and 6.0 $mmol^{-1}$ tartaric acid solution at 1.0 mL min^{-1} were used without the suppressor system.

The amount of residual oxidant was determined using the spectrophotometric method adapted from the work of Liang *et al.* [25]. Briefly, 2.9 mL of a 0.6 mol L^{-1} KI solution and 0.06 mol L^{-1} $NaHCO_3$ solution were added to 1.0 mL of sample previously filtered. The resulting solutions were hand-shaken and allowed to equilibrate for 15 min before analysis in a UV-Vis spectrophotometer (Shimadzu UV-1800) at 352 nm.

Total organic carbon concentration ([TOC]) was measured with a GE Sievers Innovox analyzer. The [TOC] determination was performed after mixing a diluted volume of sample with $Na_2S_2O_8$ (30% *m/V*) and H_3PO_4 (6 mol L^{-1}) solutions. The TOC content was analyzed by subtraction of the measured values of inorganic and total carbon, in terms of produced CO_2. More experimental details can be found in our previous works [26, 27].

To identify the main working oxidant species, ESR tests were also carried out using DMPO and TEMP solutions as spin probes to confirm the presence of radicals (mainly $HO^{\bullet}$) and non-radicals ($^1O_2$) oxidant species, respectively. The ESR measurements were performed in an E-109 X-band Varian system spectrometer, using a rectangular cavity at room temperature. A 200 μL flat quartz cell was used to analyze samples. To elucidate the chemical structure of the main byproducts resulting from DMPO oxidation, UHPLC-QToF MS analyses were carried out. All these experimental details can be seen in Text S2, in the supplementary material section.

3. Results and discussion

3.1. Characterization of MnOOH

Fig. 1a shows TEM images of the as-prepared MnOOH oxyhydroxide compound. The morphology of the catalyst exhibited a rod-like structure with a length and diameter ranging from 130 to 270 nm and 20–30 nm, respectively, corroborating the work of Crisostomo *et al.* [22]. To confirm the crystallinity of MnOOH nanoparticles HRTEM micrography can be seen in Fig. 1b. The lattice fringe spacing was close to 3.4 Å, corresponding to the $(11\bar{1})$ diffraction plane of MnOOH [22].

Fig. S2 shows the XRD of the as-prepared catalyst on which the diffraction pattern can be indexed to the ICSD card number 98–008–4949. No impurities were observed in the XRD pattern.

To further confirm the surface composition of the MnOOH, XPS analyses were performed. As shown in Fig S3, the high-resolution C 1s spectrum was deconvoluted into four peaks related to hydrocarbons (C–H) at 284.8 eV and oxygenated groups of alcohol/ether (C–O type at 286.2 eV), carbonyl (C═O at 287.8 eV), and carboxyl (–O–C═O at 289.4 eV) [28]. The presence of carbon functional groups is typical for *ex situ* analysis and derives mainly from physiosorbed surface contamination. However, it cannot be excluded that part of these functional groups, such as carboxyl was attached to the catalyst during the synthesis procedure and during longer treatment periods. These functional groups have to be taken into account in terms of the adsorption performance of MnOOH [29], as discussed below. The signals of O 1s were resolved into four peaks, as can be seen in Fig. 2a. The main components of all spectra are related to O–Mn (O^{-2}) type bonds at 529.5 eV and hydroxyl groups (HO–Mn) on the oxide/hydroxyl near surface at 530.8 eV [28]. In addition, the components of oxygenated groups at 530.8 eV (O═C), 532.1 eV (O–C), and 533.1 eV (O–C═O) were previously identified in the C 1s spectrum. Besides, the peaks of Mn $2p_{3/2}$ spectrum (Fig. 2b) were resolved into four peaks corresponding to MnO (640.7 eV), $MnOOH/Mn_2O_3$ (642.1 eV), MnO_2 (643.5 eV), and MnO_3 (645.0 eV) [28]. The above results confirm the successful synthesis of MnOOH.

3.2. Catalytic performance evaluation

3.2.1. Performance of MnOOH/PMS system on CIP decomposition

Fig. 3 shows the evolution of the remaining fraction of CIP and TOC as a function of treatment time using 1.0 g L^{-1} of MnOOH and PMS at pH 3.0. The catalytic activity and adsorption performance of MnOOH were

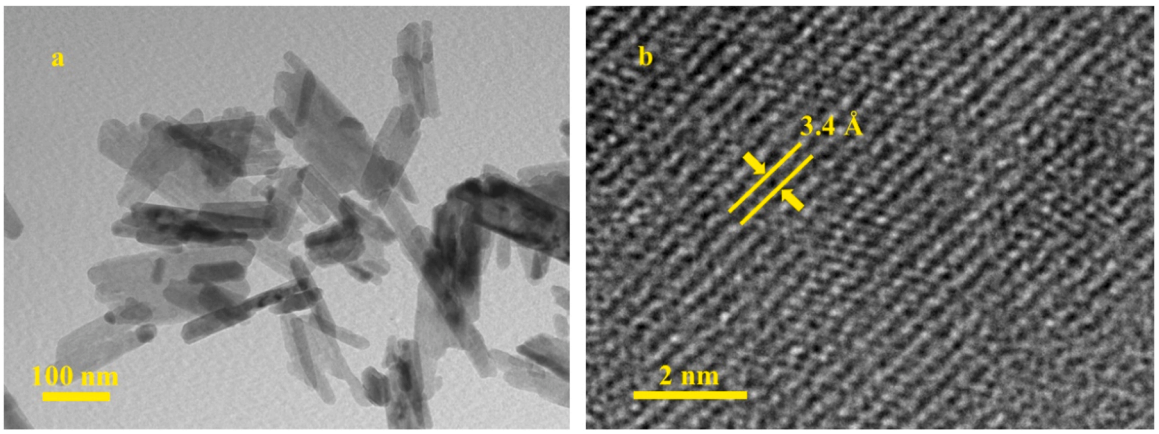

Fig. 1. **a)** Transmission electron microscope (TEM) image and **b)** high-resolution TEM (HRTEM) of the as-prepared MnOOH.

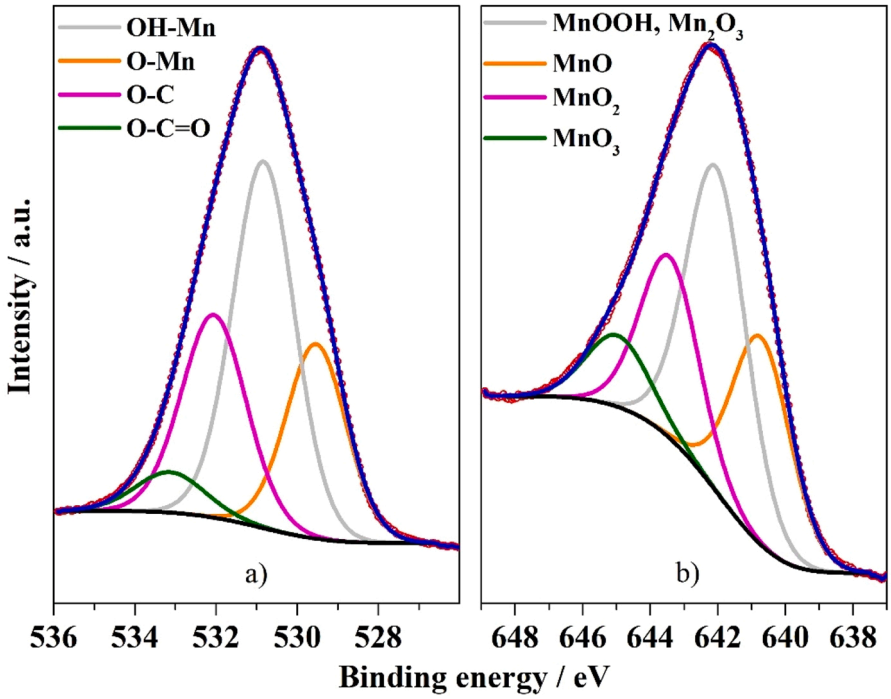

Fig. 2. High-resolution XPS spectra of **a)** O 1s and **b)** Mn $2p_{3/2}$ for the MnOOH compound for the as-prepared MnOOH .

first monitored. As can be observed in Fig. 3a, ~25% CIP was adsorbed and/or oxidized in MnOOH after 6 h (see discussion below), which is likely due to hydrogen bonding between pollutant and the oxygen-containing functional groups in the catalyst, such as hydroxyl [30,31]. The sole use of PMS led to 80% of CIP oxidation and only 10% of CO_2 conversion at the same treatment time (the observed TOC values fluctuation is quite common when low abatement values are attained [32, 33]). That behavior is probably due to the direct hydroxylation/dealkylation reaction on the piperazine ring of CIP by PMS [34, 35]. When catalyst and PMS were combined, the CIP molecule was completely oxidized in 3 h, whereas 60% of mineralization was achieved. To confirm whether the coupling was synergistic or not, CIP and TOC removal levels for the uncombined experiments (control experiments) were summed, as represented by the dashed line (named as theoretical line) in Fig. 3. As the CIP and TOC removal levels using the MnOOH/PMS system were higher than the theoretical line (control experiments), a synergistic process was confirmed due to the *in situ* activation of PMS by MnOOH to produce powerful oxidizing species (see below).

3.2.2. *Effects of solution pH*

The solution pH is a significant factor affecting the catalytic performance of heterogeneous reactions. Thus, an investigation into the effect of different pH conditions (3.0, 7.0, and 10.0) towards CIP oxidation and mineralization was conducted. Complete oxidation of CIP was attained in all studied pH conditions (~100% in 3 h), as seen in Fig. 4; however, a slight increase in the pseudo-first order kinetic constant from acidic to alkaline solutions was observed, as can be seen in Table S1. That behavior can be explained considering *i*) the dependence of the CIP species reactivity with solution pH (*i.e.*, cationic, zwitterion/neutral, or anionic – pK_{a1} and pK_{a2} is equal to 6.09 and 8.62 [36], respectively) as reported by Zhou *et al.* [35] – in that work (only using CIP and PMS), the anionic and zwitterion/neutral species (pH > 7) were more susceptible to PMS (pK_a = 9.4 [37]) oxidation due to the higher reactivity of the secondary amine in the piperazine ring – and *ii*) to the fact that at alkaline solutions, $^1O_2$ oxidizing species can be also produced (Eq. 5) [38], leading to a superior oxidation level. Now, taking into account the contribution mediated by the activated PMS with MnOOH, acidic solutions are expected to have an improved performance than at alkaline

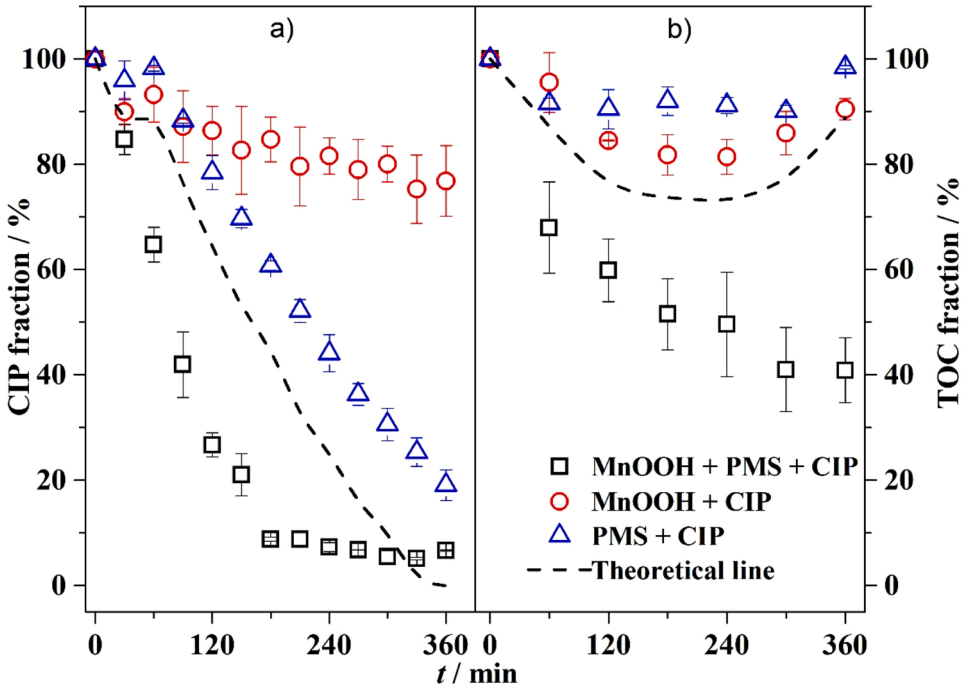

Fig. 3. Remaining fraction of CIP (CIP fraction) and TOC (TOC fraction) as a function of treatment time (*t*) for (○) adsorption performance of MnOOH, (△) oxidation by PMS alone, and (□) oxidation by the MnOOH/PMS system. The theoretical line is based on the sum of uncombined experiments (- -). Conditions: 50 mg L^{-1} CIP, 1.0 g L^{-1} MnOOH, 1.0 g L^{-1} PMS, pH 3.0, and 25 °C. Error bars refer to two repetitions.

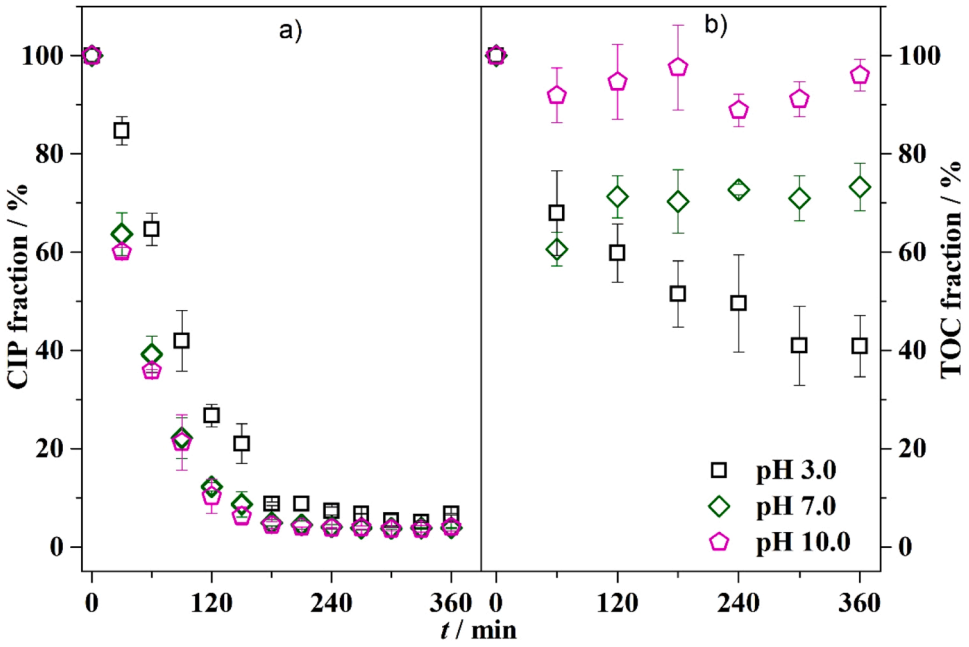

Fig. 4. Remaining fraction of CIP (CIP fraction) and TOC (TOC fraction) as a function of treatment time (*t*) at distinct pH values: (□) 3.0; (◇) 7.0; (⬠) 10.0. Conditions: 50 mg L^{-1} CIP, 1.0 g L^{-1} MnOOH, 1.0 g L^{-1} PMS, and 25 °C. Error bars refer to two repetitions.

conditions due to surface charge repulsion (see discussion below). The last process might be more appropriate for similar rates of CIP oxidation (through PMS activation) from acidic to alkaline conditions than the one reported by Zhou *et al.* [35], *i.e.* without PMS activation. It is also important to highlight that any structural modification of CIP can lead to a signal loss during HPLC analyses and, therefore, the amount of oxidant is crucial.

$$HSO_5^- + SO_5^{2-} \rightarrow {}^1O_2 + 2SO_4^{2-} + H^+ \quad (5)$$

An opposite effect was observed during TOC removal, *i.e.*, acidic solutions led to superior mineralization levels and rates, as the type of oxidant (particularly, $SO_4^{\bullet-}$ and $HO^{\bullet}$ and not $^1O_2$) is essential to convert CIP and its byproducts to CO_2. That behavior can be explained by *i*) the surface charge of MnOOH, since metal oxides/hydroxides show a pH-dependent surface charging and *ii*) reactions mediated by $^1O_2$. As the pH for the point of zero charge (pH_{pzc}) was *ca.* 6.5 (see Fig. S4), which is consistent with available literature [39], it is expected that when the solution pH was over this value (7.0 and 10.0), the MnOOH surface

charge was negative. So, PMS activation by MnOOH might be hindered due to electrostatic repulsion. Likewise, at basic conditions the observed oxidation without significant CO_2 conversion is due to the produced low power $^1O_2$ species (Eq. 5) specially at pH 10 [38].

To assess the possible effect of homogeneous reaction mediated by Mn(II) species leaching from the MnOOH compound at acidic conditions, ion chromatography experiments were carried out. As seen in Fig. S5, high levels (~350 mg L^{-1}) of Mn(II) were detected in the absence of PMS (only MnOOH and MnOOH+CIP – the last is probably due to a redox reaction between Mn(III)/Mn(IV) species with the piperazine group in CIP as described in [39,40]). When using PMS, independently of the organic compound, low Mn(II) leaching values were measured (~25 mg L^{-1}). On the solid surface, Mn(II) reduces PMS resulting in the formation of $SO_4^{\bullet-}$/$HO^{\bullet}$ and MnO_2 (*i.e.*, Mn(IV) and catalyst deactivation) as already described elsewhere [39,41,42]. In solution, the possible formation of unstable Mn(III) from Mn(II) species (Eqs. 6 and 7) can lead to a disproportionation reaction resulting in the formation of low reactive MnO_2 (Eq. 8). The Mn(III) species can also react with PMS (Eq. 9) to produce $SO_5^{\bullet-}$ species and, possibly, $^1O_2$ (Eq. 10) [43].

$$Mn^{2+} + HSO_5^- \rightarrow Mn^{3+} + SO_4^{\bullet-} + OH^- \quad (6)$$

$$Mn^{2+} + SO_4^{\bullet-} \rightarrow Mn^{3+} + SO_4^{2-} \quad (7)$$

$$2Mn^{3+} + 2H_2O \rightarrow Mn^{2+} + MnO_2 + 4H^+ \quad (8)$$

$$Mn^{3+} + HSO_5^- \rightarrow Mn^{2+} + SO_5^{\bullet-} + H^+ \quad (9)$$

$$2SO_5^{\bullet-} + H_2O \rightarrow 2HSO_4^- + 1.5\,^1O_2 \quad (10)$$

To investigate the possible effect of homogeneous reactions at acidic conditions, experiments were carried out in solutions intentionally contaminated with Mn(II) and without the solid MnOOH catalyst. As seen in Fig. S6, no significant oxidation or mineralization levels for CIP were observed in the presence of Mn(II) species, suggesting a negligible contribution of homogeneous reactions. A similar behavior was observed in the work of Anipsitakis and Dionysiou [41], in which distinct transition metallic ions (Co(II), Ce(III), Mn(II), Ni(II), Ru(III), and V(III)) were tested for the activation of H_2O_2, PMS (HSO_5^-) and PDS ($S_2O_8^{2-}$). In the case of Mn(II) ions, PMS can be activated leading to trapped sulfate radicals, as represented by Eq. 11.

$$Mn^{2+} + HSO_5^- \rightarrow [Mn^{III}(SO_4^{\bullet-})]^{2+} + OH^- \quad (11)$$

3.2.3. *Effect of PMS and MnOOH concentration*

The effects of PMS (1.0 – 4.0 g L^{-1}) and MnOOH (0.5 – 2.0 g L^{-1}) concentration on CIP oxidation and mineralization were investigated, as seen in Fig. 5. As expected, the oxidation levels and rates (see Table S2) of CIP were enhanced at increasing concentrations of PMS. However, no significant differences for the CIP mineralization levels and rates were observed. A maximum of ~60% TOC removal was attained after 6 h. That behavior might be caused by the insufficient active sites on the MnOOH surface, which limits the PMS activation. The use of PMS concentrations higher than 1 g L^{-1} can also result in an excess of unreacted oxidant (~30% and ~50% when using 2 and 4 g L^{-1}, respectively, of PMS), as can be seen in Fig. S7 for the experiments showed in Fig. 5.

The investigation of MnOOH concentration has not led to any significant oxidation levels and rates of CIP from 0.5 to 2.0 g L^{-1} (see Fig. 6), which confirms the hypothesis that the degradation of CIP is mainly influenced by oxidation with PMS. For TOC removal, a slight increase of 20% was noticed when the MnOOH concentration increased from 0.5 to 1.0 g L^{-1} after 6 h, without further increments at 2.0 g L^{-1}. This result was not expected, since by increasing the amount of catalyst, a higher number of adsorption sites available for PMS activation would be expected. That behavior may be due to the agglomeration of MnOOH particles found in solution, leading to no effective increment in the active area. Similar results were also reported for distinct heterogeneous systems [44,45].

Thus, the optimized conditions were acidic solutions (pH 3.0) using 1.0 g L^{-1} of MnOOH and PMS at 25 °C, including TOC removal. The remaining analyzes were carried out at the same conditions.

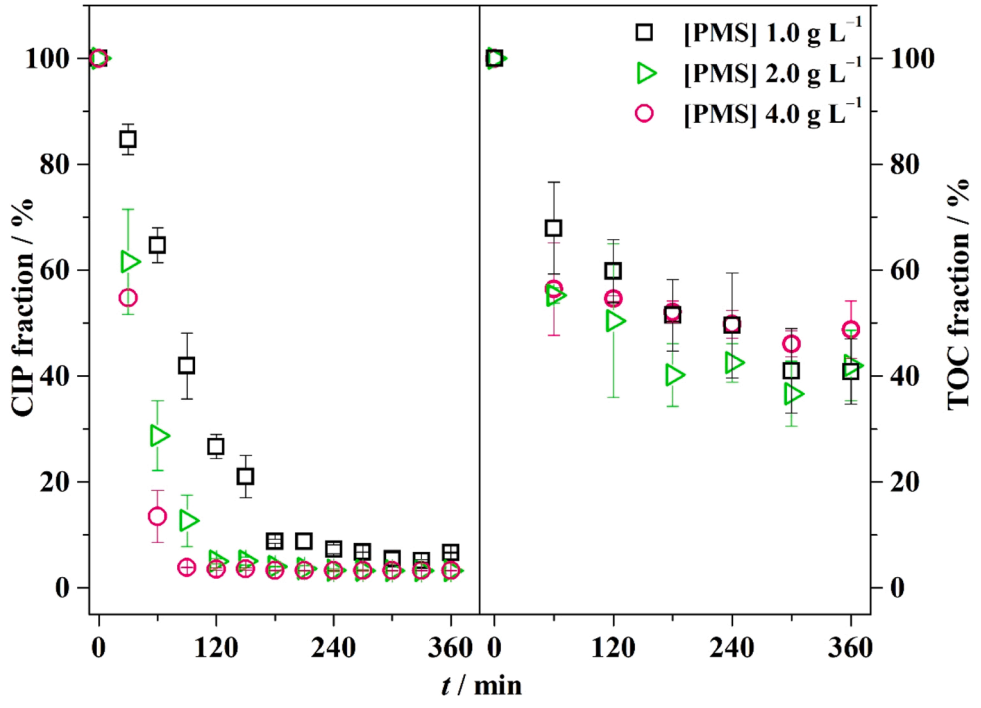

Fig. 5. Remaining fraction of CIP (CIP fraction) and TOC (TOC fraction) as a function of treatment time (*t*) at distinct PMS concentration values: (□) 1.0, (▷) 2.0, and (○) 4.0. g L^{-1}. Conditions: 50 mg L^{-1} CIP, 1.0 g L^{-1} MnOOH, pH 3.0, and 25 °C. Error bars refer to two repetitions.

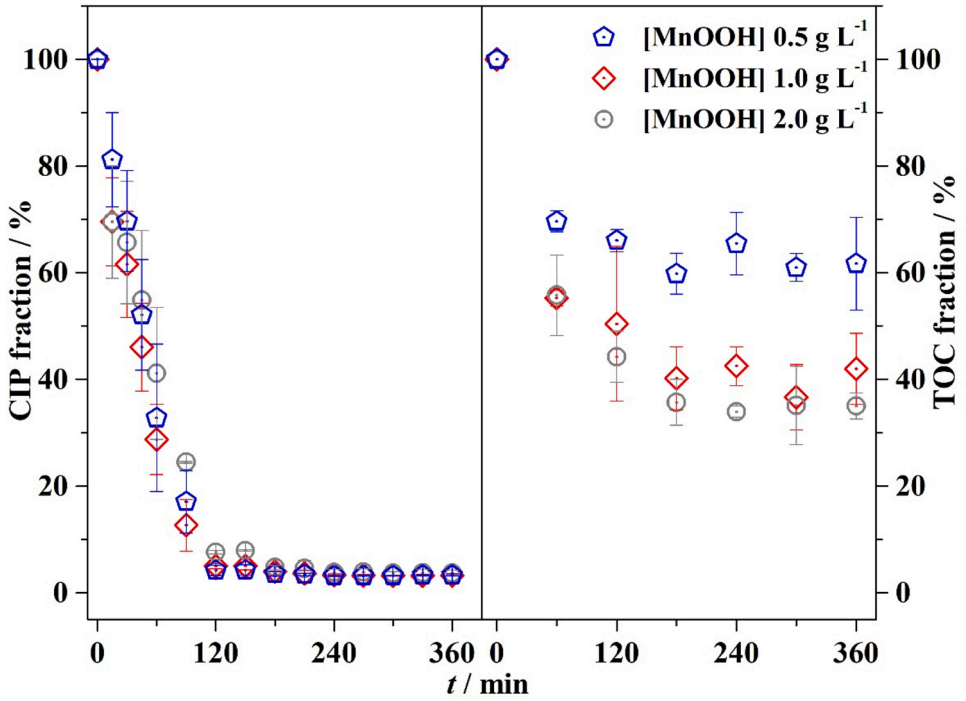

Fig. 6. Remaining fraction of CIP (CIP fraction) and TOC (TOC fraction) as a function of treatment time (*t*). Effect of MnOOH concentration: (⬠) 0.5 g L^{-1}; (◇) 1.0 g L^{-1}; (○) 2.0. g L^{-1}. Conditions: 50 mg L^{-1} CIP, 2.0 g L^{-1} PMS, pH 3.0, and 25 °C. Error bars refer to two repetitions.

3.3. CIP degradation products and pathways: UHPLC-QToF MS and carboxylic acid determinations

For the optimized condition and considering the high levels of conversion to CO_2, only five intermediates were identified (see Table S3 for the *m/z* values and Fig. S8 for the total ion chromatographic profiles) using a UHPLC-QToF MS system (see Fig. S9 for the MS/MS spectra of intermediates showed in Table S3). Fig. 7 shows the proposed

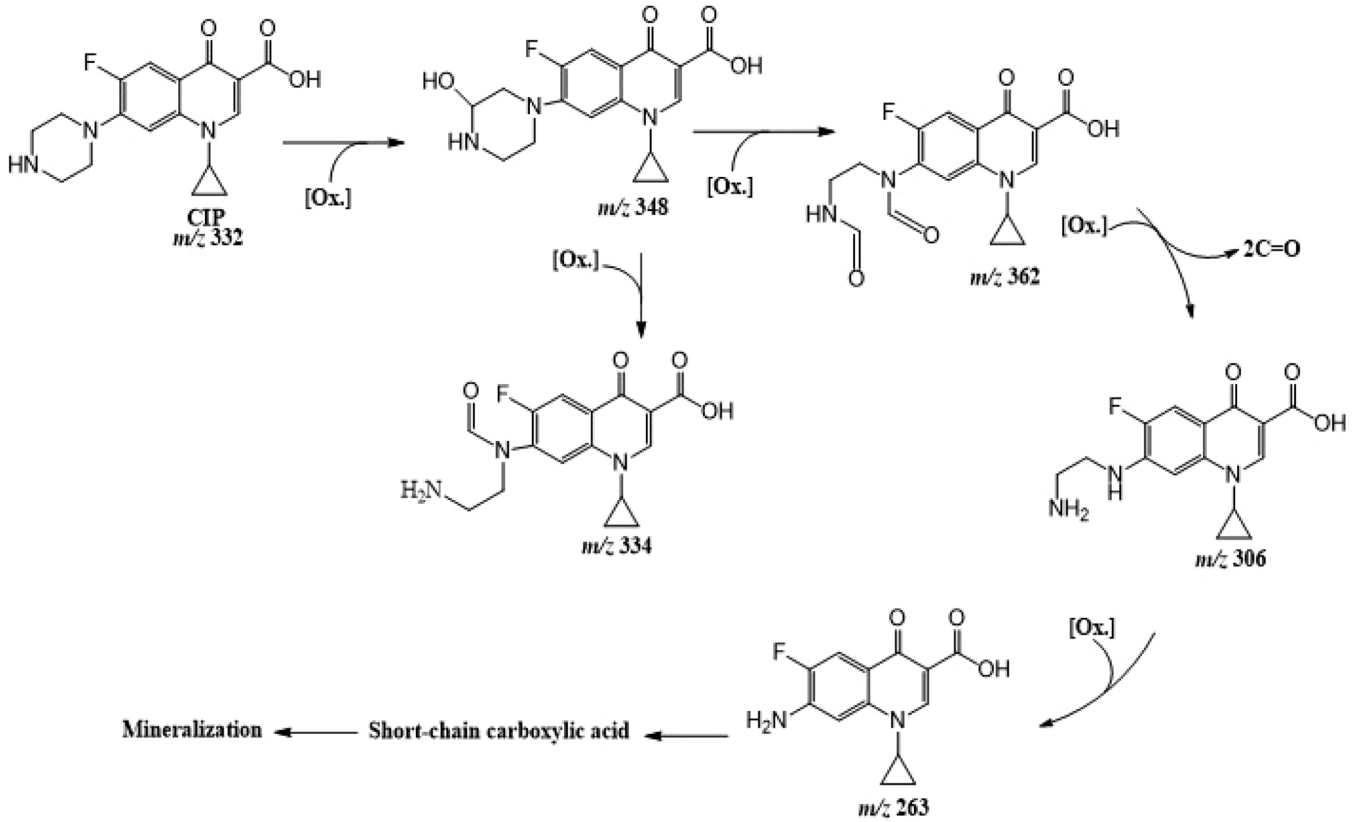

Fig. 7. Proposed degradation pathways of CIP in the MnOOH/PMS system. Conditions: 50 mg L^{-1} CIP, 1.0 g L^{-1} PMS, 1.0 g L^{-1} MnOOH, pH 3.0, and 25 °C.

degradation route, in which oxidation (probably mediated by $HO^{\bullet}$, $SO_4^{\bullet-}$, and $^1O_2$) is initiated on the side chain of the piperazine group due to its high electron density [46] resulting in products with *m/z* 334.1198, 348.1355, and 362.1147. After successive loss of two formaldehyde groups followed by an amine group, byproducts with *m/z* 306.1258 and 263.0827 were produced, respectively. In the final stages of CIP oxidation, the production of carboxylic acids (mainly formic, acetic, propionic, and adipic acids – see Fig. S10) clearly indicates the breakdown and oxidation of the aromatic ring as well as the piperazine moiety before complete conversion to CO_2. The presence of F^- ion species was investigated; however, no reliable concentration values were obtained due to interferences in the baseline of the conductivity measurements promoted by the PMS salt precursor.

3.4. Identification of the main working oxidants

The ESR spectrum resulting from the reaction of MnOOH, PMS, and DMPO is displayed in Fig. S11. An intense resonance triplet line (1:1:1) was observed from N magnetic dipole moment resulting from two consecutive addition reactions in the adjacent alpha carbon atom. A less intense resonance line split into a 1:2:2:1 was also observed and attributed to the DMPO-OH compound (DMPO-SO_4 is unstable and easily hydrolyzed [47]). The hyperfine constant $a^H = a^N = 16.1$ G is slightly higher than the more common 14.9 G probably due to the variable ionic strength and solution pH close to 10 [48]. To elucidate the main oxidation byproducts resulting from DMPO oxidation new ESR measurements were performed with small field modulation to resolve the superhyperfine splitting. The result suggests that the superhyperfine splitting is compatible with nuclear spin from three equivalent hydrogens of the CH_3 group and two equivalent hydrogens from two OH groups to unpaired electron on NO fragment indicating the DMPO-$(OH)_2$ adduct (see Fig. S12). To confirm the latter possibility, UHPLC-QToF MS measurements were also carried out as previously described. As can be seen in the extracted ion chromatogram of Fig. S13 and in the MS/MS spectra of Fig. S14, DMPO-OH (*m/z* 130.0860) and DMPO$(OH)_2$ (*m/z* 148.0966) compounds were detected. The proposed fragmentation route for each compound is depicted in Fig. S15, in agreement with studies of Domingues *et al.* [49], Guo *et al.* [50], and Pavlovic & Hopke [51]. Thus, the triplet signal results from two consecutive addition reactions involving $HO^{\bullet}$ radicals. For the experiments using TEMP, the results were not conclusive as the characteristic triplet (1:1:1) was observed in the control experiment using PMS (1.0 g L^{-1}). Hence, only small modifications were observed when using MnOOH and PMS (see the characteristic triplet signals in Fig. S16).

3.5. Time evolution of MnOOH: morphological, structural, and electrical analyses

To investigate and understand the morphological, structural, and electric changes taking place in the MnOOH catalyst during the CIP degradation in the presence of PMS, XPS, TEM, cyclic voltammetry, electrochemical impedance, and Mn average oxidation state analyses were carried out before (as-prepared MnOOH) and after 3 h (3-MnOOH) and 6 h (6-MnOOH) of treatment in the optimized conditions.

The deconvoluted high-resolution XPS C 1s spectra for the MnOOH at distinct conditions (as-prepared and after 3 and 6 h of treatment) are displayed in Fig. S17. As mentioned above, the assigned carbon functional groups are typical for surface contamination, as the technique probes about 5 nm thick surface layer. For the 6 h sample, $–CO_3$/$–CO_2$ and $–CF_2$/$–CF_3$ termination groups appear at 289.9 eV and 292.1 eV, respectively. The presence of fluorine groups, also identified by the appearance of the F 1s signal (~0.3 at% for the 6-MnOOH and 0.2 at% for the 3-MnOOH) at ~689 eV (not shown) is interesting and may indicate a direct electron transfer from MnOOH to the CIP molecule through the piperazine moiety. That behavior is corroborated by the *i*) presence of Mn(II) species detected in the treating solution which might be produced through electron transfer reactions between the piperazine moiety of CIP and MnOOH – see [39,40] for more details and *ii*) adsorption/oxidation of CIP using MnOOH without oxidant – see Fig. 3a. The main components of the O 1s spectra at 529.5 eV and 530.8 eV are related to O–Mn bonds (O^{-2} species) and hydroxylic groups on the oxide/hydroxide surface, respectively (see Fig. 8a). In addition, there are contributions of oxygenated groups resulting from contamination by hydrocarbons (O–C at ~532.1 eV and O–C═O at ~533.1 eV), previously identified in the C 1s spectra. For the 6-MnOOH sample, a $–CO_3$ type termination at 531.8 eV and a high binding energy component (534.6 eV) were attributed to molecular H_2O.

Some important features can be extracted from the XPS C 1s an O 1s spectra for different collection times: *i*) a significant increase of the peak area related to the O–Mn bonds, from 23.4% (as-prepared) to 37.3% (3 h) and 39.1% (6 h), *ii*) subsequently a decrease of the HO–Mn components, from 45.0% (as-prepared) to 44.9% (3 h) and 25.0% (6 h), and *iii*) appearance of new intensities after 6 h treatment, related to $–CO_3$ and $–CF_2$/$–CF_3$ terminations. These findings suggest that MnOOH is oxidized to higher oxidation states (inactivation process), possibly supplying electrons to the oxidant (main process), and activating both PMS and the CIP molecule. As a result of the MnOOH inactivation, an outside-in conversion reaction may take place, that is, forming a core-shell compound of Mn(III) covered by an oxide layer of higher oxidation states after 6 h of treatment. This finding is supported by the observed decrease in the TOC removal rate and cessation of oxidant consumption after ~3 h, as shown below. The inactivation is probably caused by the thickening of the oxide layer that hinders the electron transfer to PMS (see discussion below). Moreover, the $–CF_2$/$–CF_3$ termination seems to confirm a direct electron transfer from MnOOH to CIP after a first phase of the adsorption process (see red circle in Fig. 3a).

To obtain more information on the inactivation process, Mn $2p_{3/2}$ spectra were fitted with 4 and 5 components corresponding to different oxidation states of Mn (see Fig. 8b). For the as-prepared sample, the predominant intensity is related to MnOOH (or Mn_2O_3) at 642.1 eV with 44.6% peak area, followed by MnO_2 at 643.5 eV (23.4%), MnO at 640.7 eV (22.9%), and MnO_3 at 645.0 eV (9.1%). For the 3-MnOOH sample, initially a partial reduction process takes place increasing the fraction of the MnO phase, probably due to the initial leaching of Mn(III) ions. However, the 6-MnOOH sample shows an increase of the oxidation on the sample surface after 6 h. The intensity of the MnO_3 oxidation state increases on the expense of MnOOH, accompanied by the appearance of a new intensity at 536.6 eV attributed to the Mn_2O_7 phase. These results are consistent with O 1s data, and find evidence of a significant decrease of the MnOOH phase (44.6–23.4%) during CIP degradation.

To further understand the evolution of Mn average oxidation state potentiometric titration experiments were carried out. As shown in Table S4, the average oxidation state of Mn in the as-prepared sample increased from 3.02 to 3.26 after 3 h and then to 3.36 after 6 h of treatment. The result confirms that Mn(II) in the MnOOH compound is being gradually oxidized to Mn(IV) species and transferring electrons to CIP, but mainly to PMS. Such structural transformation was not confirmed by XRD whose diffraction pattern remained close to that of the as-prepared MnOOH (Fig. S18). However, upon visual inspection of the assayed MnOOH compound, it can be readily attested that a color change from brown to black occurred (Fig. S19).

HRTEM images of the as-prepared and 3-MnOOH confirm the appearance of an amorphous phase (shell) in the outer region of the MnOOH as seen in Fig. 9a, in contrast to a crystalline region in the inner part of the particle. Note that such structure, *i.e.*, core-shell, was not observed in the as-prepared MnOOH (see the aligned fringes throughout the particle of Fig. 9b).

CV measurements (20 mV s^{-1} and 2nd scan) for the 3-MnOOH, 6-MnOOH, and as-prepared are shown in Fig. S20. The electrochemical profile of the as-prepared sample is characterized by a capacitive behavior without clear oxidation and reduction peaks. That behavior is

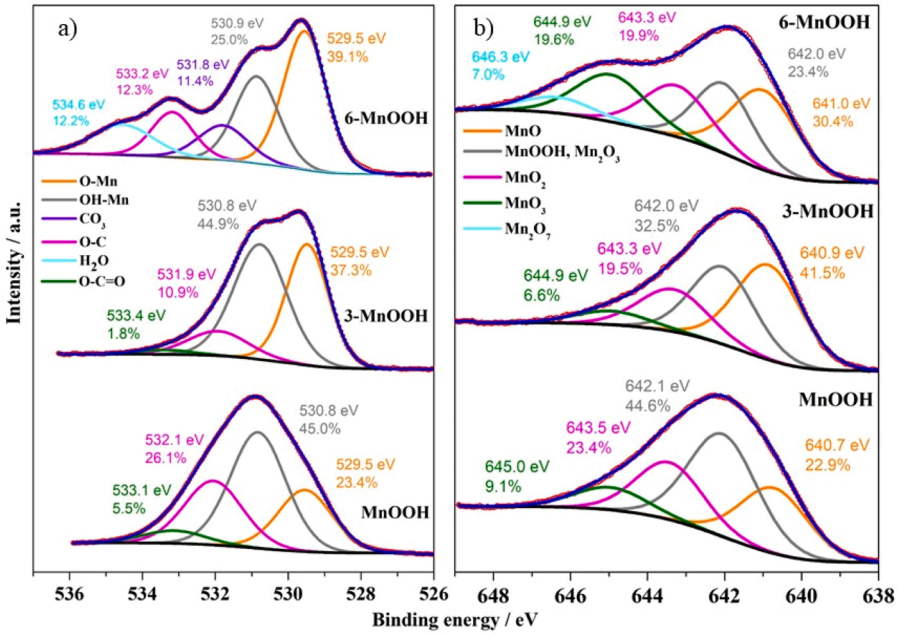

Fig. 8. High-resolution XPS spectra of **a)** O 1s and **b)** Mn $2p_{3/2}$ for MnOOH at distinct conditions: as-prepared (MnOOH), after 3 h (3-MnOOH), and 6 h (6-MnOOH) of treatment. Conditions: 50 mg L^{-1} CIP, 1.0 g L^{-1} MnOOH, 1.0 g L^{-1} PMS, pH 3.0, and 25 °C).

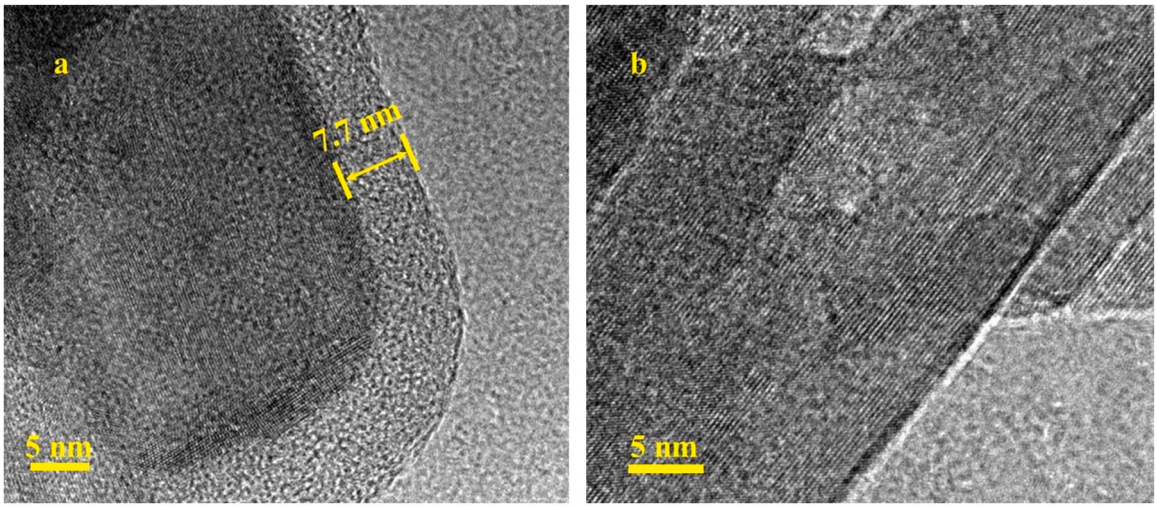

Fig. 9. High-resolution TEM (HRTEM) for MnOOH at distinct conditions: **a)** after 3 h (3-MnOOH) of treatment and **b)** as-prepared (MnOOH). Conditions: 50 mg L^{-1} CIP, 1.0 g L^{-1} MnOOH, 1.0 g L^{-1} PMS, pH 3.0, and 25 °C.

different from the one of 3-MnOOH and 6-MnOOH samples, in which an oxidation (0.98 V *vs.* Ag/AgCl/KCl (3 mol L^{-1})) and reduction (0.81 V *vs.* Ag/AgCl/KCl (3 mol L^{-1})) peaks (Mn(III) to Mn(IV) with Na^+ ion intercalation) can be clearly seen due to the produced MnO_2 from reaction with PMS oxidant. The electrochemical impedance of those samples is displayed in Fig. S21. The equivalent circuit used to obtain the best fits of the experimental data was composed of the solution resistance (R_{sol}), carbon material charge transfer resistance (R_C), and the oxide charge transfer resistance (R_{oxide}) at high and medium to low frequencies, respectively. The constant phase elements CPE_C are in parallel with the R_C element and CPE_{Oxide} with the double layer from the oxide material at medium to low frequencies, respectively. The time evolution of the R_{oxide} for the as-prepared, 3-MnOOH, and 6-MnOOH shows in Fig. S22 a resistance increase from 2.9 $\pm$1.0 $\times$ 10^4 Ω (as-prepared) to 6.8 $\pm$2.7 $\times$ 10^4 Ω (6 h), during PMS activation mediated by MnOOH, hindering further oxidant activation. This is also seen by the increase of the impedance modulus when comparing the 6-MnOOH with the as-prepared sample (Fig. S21b).

Taking into account the *post mortem* analyses, a decrease in the efficiency of the MnOOH/MnO_2 compound during the recycling test would be expected. However, from the second until the fifth run, the oxidation of CIP remained close to the results of the as-prepared material, as seen in Fig. S23. During such experiments and after adding PMS, the black MnOOH/MnO_2 composite turned to the brown color, similar to the as-prepared material. As discussed in detail in the work of Li *et al.* [52], this might indicate that Mn(IV) was reduced by adsorbed PMS to Mn(III) whose degree will certainly depend on the PMS concentration and oxide termination groups. Further studies will be carried out to understand that behavior.

4. Conclusions

Nanometric MnOOH oxyhydroxide was successfully synthesized using a less harmful and greener reductor to activate peroxymonosulfate (PMS) oxidant under acidic conditions. In the optimized experimental condition, within 3 h a complete oxidation of CIP antibiotic with more than 60% mineralization within 6 h was attained, without contributions from homogeneous reactions (*i.e.*, Mn(II) species). A low number and intensity of intermediate compounds were detected by UHPLC-QToF MS due to the high oxidizing conditions leading to the production of carboxylic acid and inorganic ions. The latter specie was only detected by XPS on the surface of MnOOH after 6 h treatment. Thus, the CIP molecule might be oxidized through *i*) PMS activation promoted by MnOOH resulting in $HO^{\bullet}$ radicals and, to a minor extent, *ii*) directly on the MnOOH surface through direct electron transfer. The preceding result was confirmed by ESR measurements and structural changes that took place on the MnOOH surface, *i.e.*, an increase of the oxidation state of Mn oxides at the expense of MnOOH, as evidenced by XPS and potentiometric titration. The Mn oxidation led to the formation of an amorphous shell structure of MnO_2 and MnO_3 over the MnOOH crystallites with the subsequent increase of the charge transfer resistance that hindered the electron transfer to the PMS oxidant or CIP byproducts. Apparently, these behaviors seem to be recovered when using a freshly prepared PMS solution. These findings may shed light on the synthesis of improved/engineered compounds to activate oxidants.

CRediT authorship contribution statement

Yeison Núñez-de la Rosa: Formal analysis, Investigation, Data curation, Writing – original draft, Writing – review & editing, Visualization. **Luis Guillermo Cuadrado Durango**: Formal analysis, Investigation, Data curation, Writing – review & editing, Visualization. **Moacir Rossi Forim**: Resources, Writing – review & editing, Visualization, Supervision, Funding acquisition. **Otaciro Rangel Nascimento**: Formal analysis, Investigation, Resources, Data curation, Writing – review & editing, Visualization, Funding acquisition. **Peter Hammer**: Formal analysis, Investigation, Resources, Data curation, Writing – review & editing, Visualization, Supervision, Funding acquisition. **José M. Aquino**: Formal analysis, Resources, Writing – original draft, Writing – review & editing, Visualization, Supervision, Project administration, Funding acquisition.

Declaration of Competing Interest

The authors declare that they have no known competing financial interests or personal relationships that could have appeared to influence the work reported in this paper.

Data availability

Data will be made available on request.

Acknowledgements

Financial support and scholarships from the Brazilian funding agencies: São Paulo Research Foundation – FAPESP (#2014/50918-7 and #2019/07943-4), National Council for Scientific and Technological Development – CNPq (#465357/2014-8, #302186/2019-0, #305943/2020-0, #406537/2021-6, and #307800/2021-0), Coordination of Superior Level Staff Improvement – Capes (Finance Code 001), and Finep (0152/21 - MARTMA) are gratefully acknowledged. The authors also thank the Laboratory of Structural Characterization (LCE/DEMa/UFSCar) for the general facilities.

Appendix A. Supporting information

Supplementary data associated with this article can be found in the online version at doi:10.1016/j.apcatb.2023.122439.

References

[1] A. Getirana, R. Libonati, M. Cataldi, Brazil is in water crisis — it needs a drought plan, Nature 600 (2021) 218–220, https://doi.org/10.1038/d41586-021-03625-w.
[2] V.A. Tzanakakis, N.V. Paranychianakis, A.N. Angelakis, Water supply and water scarcity, Water 12 (2020) 2347, https://doi.org/10.3390/w12092347.
[3] A. Saravanan, P. Senthil Kumar, S. Jeevanantham, S. Karishma, B. Tajsabreen, P. R. Yaashikaa, B. Reshma, Effective water/wastewater treatment methodologies for toxic pollutants removal: processes and applications towards sustainable development, Chemosphere 280 (2021), 130595, https://doi.org/10.1016/j.chemosphere.2021.130595.
[4] L.G. Kahn, K.G. Harley, E.L. Siegel, Y. Zhu, P. Factor-Litvak, C.A. Porucznik, M. Klein-Fedyshin, A.E. Hipwell, Persistent organic pollutants and couple fecundability: a systematic review, Hum. Reprod. Update 27 (2021) 339–366, https://doi.org/10.1093/humupd/dmaa037.
[5] L. Le Coadou, K. Le Ménach, P. Labadie, M.-H. Dévier, P. Pardon, S. Augagneur, H. Budzinski, Quality survey of natural mineral water and spring water sold in France: monitoring of hormones, pharmaceuticals, pesticides, perfluoroalkyl substances, phthalates, and alkylphenols at the ultra-trace level, Sci. Total Environ. 603–604 (2017) 651–662, https://doi.org/10.1016/j.scitotenv.2016.11.174.
[6] S.J. Chow, N. Ojeda, J.G. Jacangelo, K.J. Schwab, Detection of ultrashort-chain and other per- and polyfluoroalkyl substances (PFAS) in U.S. bottled water, Water Res. 201 (2021), 117292, https://doi.org/10.1016/j.watres.2021.117292.
[7] J. Borrull, A. Colom, J. Fabregas, E. Pocurull, F. Borrull, A liquid chromatography tandem mass spectrometry method for determining 18 per- and polyfluoroalkyl substances in source and treated drinking water, J. Chromatogr. A 1629 (2020), 461485, https://doi.org/10.1016/j.chroma.2020.461485.
[8] M. Triassi, P. Montuori, D.P. Provvisiero, E. De Rosa, F. Di Duca, P. Sarnacchiaro, S. Díez, Occurrence and spatial-temporal distribution of atrazine and its metabolites in the aquatic environment of the Volturno River estuary, southern Italy, Sci. Total Environ. 803 (2022), 149972, https://doi.org/10.1016/j.scitotenv.2021.149972.
[9] C. Montagner, F. Sodré, R. Acayaba, C. Vidal, I. Campestrini, M. Locatelli, I. Pescara, A. Albuquerque, G. Umbuzeiro, W. Jardim, Ten years-snapshot of the occurrence of emerging contaminants in drinking, surface and ground waters and wastewaters from São Paulo state, Brazil, J. Braz. Chem. Soc. 803 (2018), 149972, https://doi.org/10.21577/0103-5053.20180232.
[10] Y. Wan, T.M. Tran, V.T. Nguyen, A. Wang, J. Wang, K. Kannan, Neonicotinoids, fipronil, chlorpyrifos, carbendazim, chlorotriazines, chlorophenoxy herbicides, bentazon, and selected pesticide transformation products in surface water and drinking water from northern Vietnam, Sci. Total Environ. 750 (2021), 141507, https://doi.org/10.1016/j.scitotenv.2020.141507.
[11] W. Guo, B. Pan, S. Sakkiah, G. Yavas, W. Ge, W. Zou, W. Tong, H. Hong, Persistent organic pollutants in food: contamination sources, health effects and detection methods, Int. J. Environ. Res. Public Health 16 (2019) 4361, https://doi.org/10.3390/ijerph16224361.
[12] D.B. Miklos, C. Remy, M. Jekel, K.G. Linden, J.E. Drewes, U. Hübner, Evaluation of advanced oxidation processes for water and wastewater treatment – a critical review, Water Res. 139 (2018) 118–131, https://doi.org/10.1016/j.watres.2018.03.042.
[13] D.R. Kearns, Physical and chemical properties of singlet molecular oxygen, Chem. Rev. 71 (1971) 395–427, https://doi.org/10.1021/cr60272a004.
[14] L. Wang, H. Xu, N. Jiang, Z. Wang, J. Jiang, T. Zhang, Trace cupric species triggered decomposition of peroxymonosulfate and degradation of organic pollutants: Cu(III) being the primary and selective intermediate oxidant, Environ. Sci. Technol. 54 (2020) 4686–4694, https://doi.org/10.1021/acs.est.0c00284.
[15] M. Kamagate, M. Pasturel, M. Brigante, K. Hanna, Mineralization enhancement of pharmaceutical contaminants by radical-based oxidation promoted by oxide-bound metal ions, Environ. Sci. Technol. 54 (2020) 476–485, https://doi.org/10.1021/acs.est.9b04542.
[16] Y. Li, W. Zhu, Q. Guo, X. Wang, L. Zhang, X. Gao, Y. Luo, Highly efficient degradation of sulfamethoxazole (SMX) by activating peroxymonosulfate (PMS) with $CoFe_2O_4$ in a wide pH range, Sep. Purif. Technol. 276 (2021), 119403, https://doi.org/10.1016/j.seppur.2021.119403.
[17] Y. Gao, Z. Chen, Y. Zhu, T. Li, C. Hu, New insights into the generation of singlet oxygen in the metal-free peroxymonosulfate activation process: important role of electron-deficient carbon atoms, Environ. Sci. Technol. 54 (2020) 1232–1241, https://doi.org/10.1021/acs.est.9b05856.
[18] J. Lee, U. von Gunten, J.-H. Kim, Persulfate-based advanced oxidation: critical assessment of opportunities and roadblocks, Environ. Sci. Technol. 54 (2020) 3064–3081, https://doi.org/10.1021/acs.est.9b07082.
[19] R. Yang, Y. Fan, R. Ye, Y. Tang, X. Cao, Z. Yin, Z. Zeng, MnO_2-based materials for environmental applications, Adv. Mater. 33 (2021) 2004862, https://doi.org/10.1002/adma.202004862.
[20] Y. Yang, P. Zhang, K. Hu, X. Duan, Y. Ren, H. Sun, S. Wang, Sustainable redox processes induced by peroxymonosulfate and metal doping on amorphous manganese dioxide for nonradical degradation of water contaminants, Appl. Catal. B Environ. 286 (2021), 119903, https://doi.org/10.1016/j.apcatb.2021.119903.

[21] Y. Liu, J. Luo, L. Tang, C. Feng, J. Wang, Y. Deng, H. Liu, J. Yu, H. Feng, J. Wang, Origin of the enhanced reusability and electron transfer of the carbon-coated Mn_3O_4 nanocube for persulfate activation, ACS Catal. 10 (2020) 14857–14870, https://doi.org/10.1021/acscatal.0c04049.
[22] V.M.B. Crisostomo, J.K. Ngala, S. Alia, A. Dobley, C. Morein, C.-H. Chen, X. Shen, S.L. Suib, New synthetic route, characterization, and electrocatalytic activity of nanosized manganite, Chem. Mater. 19 (2007) 1832–1839, https://doi.org/10.1021/cm062871z.
[23] K.J. Vetter, N. Jaeger, Potentialausbildung an der Mangandioxid-Elektrode als oxidelektrode mit nichtstöchiometrischem oxid, Electrochim. Acta 11 (1966) 401–419, https://doi.org/10.1016/0013-4686(66)80018-X.
[24] F. Cheng, J. Shen, B. Peng, Y. Pan, Z. Tao, J. Chen, Rapid room-temperature synthesis of nanocrystalline spinels as oxygen reduction and evolution electrocatalysts, Nat. Chem. 3 (2011) 79–84, https://doi.org/10.1038/nchem.931.
[25] C. Liang, C.-F. Huang, N. Mohanty, R.M. Kurakalva, A rapid spectrophotometric determination of persulfate anion in ISCO, Chemosphere 73 (2008) 1540–1543, https://doi.org/10.1016/j.chemosphere.2008.08.043.
[26] D.A.C. Coledam, I. Sánchez-Montes, B.F. Silva, J.M. Aquino, On the performance of HOCl/Fe^{2+}, HOCl/Fe^{2+}/UVA, and HOCl/UVC processes using in situ electrogenerated active chlorine to mineralize the herbicide picloram, Appl. Catal. B Environ. 227 (2018) 170–177, https://doi.org/10.1016/j.apcatb.2017.12.072.
[27] I.J.S. Montes, B.F. Silva, J.M. Aquino, On the performance of a hybrid process to mineralize the herbicide tebuthiuron using a DSA® anode and UVC light: a mechanistic study, Appl. Catal. B Environ. 200 (2017) 237–245, https://doi.org/10.1016/j.apcatb.2016.07.003.
[28] C. Powell, X-ray photoelectron spectroscopy database XPS, Version 4.1, NIST standard reference database 20 (1989), https://doi.org/10.18434/T4T88K.
[29] S.P. Varghese, A.T. Babu, B. Babu, R. Antony, γ-MnOOH nanorods: efficient adsorbent for removal of methylene blue from aqueous solutions, J. Water Process Eng. 19 (2017) 1–7, https://doi.org/10.1016/j.jwpe.2017.06.001.
[30] J. Ma, M. Yang, F. Yu, J. Zheng, Water-enhanced removal of ciprofloxacin from water by porous graphene hydrogel, Sci. Rep. 5 (2015) 13578, https://doi.org/10.1038/srep13578.
[31] Q. Wang, D. Zhou, K. Lin, X. Chen, Carbon nitride–based cuprous catalysts induced nonradical-led oxidation by peroxydisulfate: role of cuprous and dissolved oxygen, Chem. Eng. J. 419 (2021), 129667, https://doi.org/10.1016/j.cej.2021.129667.
[32] C.H.M. Fernandes, B.F. Silva, J.M. Aquino, On the performance of distinct electrochemical and solar-based advanced oxidation processes to mineralize the insecticide imidacloprid, Chemosphere 275 (2021), 130010, https://doi.org/10.1016/j.chemosphere.2021.130010.
[33] I. Sánchez-Montes, N. Wachter, B.F. Silva, J.M. Aquino, Comparison of UVC-based advanced oxidation processes in the mineralization of bisphenol A: identification of oxidation by products and toxicity evaluation, Chem. Eng. J. 386 (2020), 123986, https://doi.org/10.1016/j.cej.2019.123986.
[34] D. Ding, L. Zhou, F. Kang, S. Yang, R. Chen, T. Cai, X. Duan, S. Wang, Synergistic adsorption and oxidation of ciprofloxacin by biochar derived from metal-enriched phytoremediation plants: experimental and computational insights, ACS Appl. Mater. Interfaces 12 (2020) 53788–53798, https://doi.org/10.1021/acsami.0c15861.
[35] Y. Zhou, Y. Gao, S.-Y. Pang, J. Jiang, Y. Yang, J. Ma, Y. Yang, J. Duan, Q. Guo, Oxidation of fluoroquinolone antibiotics by peroxymonosulfate without activation: kinetics, products, and antibacterial deactivation, Water Res. 145 (2018) 210–219, https://doi.org/10.1016/j.watres.2018.08.026.
[36] P.C. Sharma, A. Jain, S. Jain, R. Pahwa, M.S. Yar, Ciprofloxacin: review on developments in synthetic, analytical, and medicinal aspects, J. Enzym. Inhib. Med. Chem. 25 (2010) 577–589, https://doi.org/10.3109/14756360903373350.
[37] Z. Yuan, M. Sui, B. Yuan, P. Li, J. Wang, J. Qin, G. Xu, Degradation of ibuprofen using ozone combined with peroxymonosulfate, Environ. Sci. Water Res. Technol. 3 (2017) 960–969, https://doi.org/10.1039/C7EW00174F.
[38] C. Qi, X. Liu, J. Ma, C. Lin, X. Li, H. Zhang, Activation of peroxymonosulfate by base: implications for the degradation of organic pollutants, Chemosphere 151 (2016) 280–288, https://doi.org/10.1016/j.chemosphere.2016.02.089.
[39] M. Kamagate, M. Pasturel, M. Brigante, K. Hanna, Mineralization enhancement of pharmaceutical contaminants by radical-based oxidation promoted by oxide-bound metal ions, Environ. Sci. Technol. 54 (2020) 476–485, https://doi.org/10.1021/acs.est.9b04542.
[40] H. Zhang, C.-H. Huang, Oxidative transformation of fluoroquinolone antibacterial agents and structurally related amines by manganese oxide, Environ. Sci. Technol. 39 (2005) 4474–4483, https://doi.org/10.1021/es048166d.
[41] G.P. Anipsitakis, D.D. Dionysiou, Radical generation by the interaction of transition metals with common oxidants, Environ. Sci. Technol. 38 (2004) 3705–3712, https://doi.org/10.1021/es035121o.
[42] J. Wang, H. B, M. Yang, R. Liu, C. Hu, H. Liu, J. Qu, Anaerobically-digested sludge disintegration by transition metal ions-activated peroxymonosulfate (PMS): comparison between Co^{2+}, Cu^{2+}, Fe^{2+} and Mn^{2+}, Sci. Total Environ. 713 (2020), 136530 https://doi.org/10.1016/j.scitotenv.2020.136530.
[43] B.-T. Zhang, L. Zhao, J.-M. Lin, Determination of folic acid by chemiluminescence based on peroxomonosulfate-cobalt(II) system, Talanta 74 (2008) 1154–1159, https://doi.org/10.1016/j.talanta.2007.08.027.
[44] S.M. Tichapondwa, J.P. Newman, O. Kubheka, Effect of TiO_2 phase on the photocatalytic degradation of methylene blue dye, Phys. Chem. Earth Parts ABC 118–119 (2020), 102900, https://doi.org/10.1016/j.pce.2020.102900.
[45] X. Han, H. Zhang, C. Zhang, Y. Zhao, N. Zhang, J. Liang, Preparation of sepiolite nanofibers supported zero valent iron composite material for catalytic removal of tetracycline in aqueous solution, Front. Chem. 9 (2021) 1–13, https://doi.org/10.3389/fchem.2021.736285.
[46] N. Wachter, J.M. Aquino, M. Denadai, J.C. Barreiro, A.J. Silva, Q.B. Cass, N. Bocchi, R.C. Rocha-Filho, Electrochemical degradation of the antibiotic ciprofloxacin in a flow reactor using distinct BDD anodes: reaction kinetics, identification and toxicity of the degradation products, Chemosphere 234 (2019) 461–470, https://doi.org/10.1016/j.chemosphere.2019.06.053.
[47] Y.-H. Guan, J. Ma, X.-C. Li, J.-Y. Fang, L.-W. Chen, Influence of pH on the formation of sulfate and hydroxyl radicals in the UV/peroxymonosulfate system, Environ. Sci. Technol. 45 (2011) 9308–9314, https://doi.org/10.1021/es2017363.
[48] Y. Kirino, T. Ohkuma, T. Kwan, Spin trapping with 5, 5-dimethylpyrroline-n-oxide in aqueous solution, Chem. Pharm. Bull. 29 (1981) 29–34, https://doi.org/10.1248/cpb.29.29.
[49] P. Domingues, M.R.M. Domingues, F.M.L. Amado, A.J. Ferrer-Correia, Detection and characterization of hydroxyl radical adducts by mass spectrometry, J. Am. Soc. Mass Spectrom. 12 (2001) 1214–1219, https://doi.org/10.1016/S1044-0305(01)00310-5.
[50] Q. Guo, S.Y. Qian, R.P. Mason, Separation and identification of DMPO adducts of oxygen-centered radicals formed from organic hydroperoxides by HPLC-ESR, ESI-MS and MS/MS, J. Am. Soc. Mass Spectrom. 14 (2003) 862–871, https://doi.org/10.1016/S1044-0305(03)00336-2.
[51] J. Pavlovic, P.K. Hopke, Technical Note: detection and identification of radical species formed from α-pinene/ozone reaction using DMPO spin trap, Atmos. Chem. Phys. Discuss. 2009 (2009) 23695–23717, https://doi.org/10.5194/acpd-9-23695-2009.
[52] H. Li, N. Yuan, J. Qian, B. Pan, Mn_2O_3 as an electron shuttle between peroxymonosulfate and organic pollutants: the dominant role of surface reactive Mn(IV) species, Environ. Sci. Technol. 56 (2022) 4498–4506,, https://doi.org/10.1021/acs.est.1c08790.